

# Strong charge-density-wave order of large-area 2D metallic $VSe_2$ nanosheets discovered by temperature-dependent Raman spectra

Cite as: Appl. Phys. Lett. **116**, 033102 (2020); <https://doi.org/10.1063/1.5135038>

Submitted: 04 November 2019 . Accepted: 10 January 2020 . Published Online: 21 January 2020

Zhen Jin (金贞), Jiaoyan Zhou, Mingzhang Xie (谢明章), Huan Ji (纪桓), Yan Ye (叶艳), Kai Jiang (姜凯), Liyan Shang (商丽燕), Jinzhong Zhang (张金中), Zhigao Hu (胡志高) , and Junhao Chu (褚君浩)



View Online



Export Citation



CrossMark

## ARTICLES YOU MAY BE INTERESTED IN

[Memristive phase switching in two-dimensional  \$1T'\$ - \$VSe\_2\$  crystals](#)

Applied Physics Letters **116**, 033101 (2020); <https://doi.org/10.1063/1.5138964>

[Thickness dependence of the charge-density-wave transition temperature in  \$VSe\_2\$](#)

Applied Physics Letters **105**, 063109 (2014); <https://doi.org/10.1063/1.4893027>

[Dirac energy spectrum and inverted bandgap in metamorphic InAsSb/InSb superlattices](#)

Applied Physics Letters **116**, 032101 (2020); <https://doi.org/10.1063/1.5128634>

Lock-in Amplifiers  
up to 600 MHz



Watch



# Strong charge-density-wave order of large-area 2D metallic VSe<sub>2</sub> nanosheets discovered by temperature-dependent Raman spectra

Cite as: Appl. Phys. Lett. **116**, 033102 (2020); doi: 10.1063/1.5135038

Submitted: 4 November 2019 · Accepted: 10 January 2020 ·

Published Online: 21 January 2020



View Online



Export Citation



CrossMark

Zhen Jin (金贞),<sup>1</sup> Jiaoyan Zhou,<sup>1</sup> Mingzhang Xie (谢明章),<sup>1</sup> Huan Ji (纪桓),<sup>1</sup> Yan Ye (叶艳),<sup>1</sup> Kai Jiang (姜凯),<sup>1</sup> Liyan Shang (商丽燕),<sup>1</sup> Jinzhong Zhang (张金中),<sup>1,a)</sup> Zhigao Hu (胡志高),<sup>1,2,3,b)</sup>  and Junhao Chu (褚君浩)<sup>1,2,3</sup>

## AFFILIATIONS

<sup>1</sup>Technical Center for Multifunctional Magneto-Optical Spectroscopy (Shanghai), Department of Materials, School of Physics and Electronic Science, East China Normal University, Shanghai 200241, China

<sup>2</sup>Collaborative Innovation Center of Extreme Optics, Shanxi University, Taiyuan, Shanxi 030006, China

<sup>3</sup>Shanghai Institute of Intelligent Electronics and Systems, Fudan University, Shanghai 200433, China

<sup>a)</sup>Electronic mail: [jzzhang@ee.ecnu.edu.cn](mailto:jzzhang@ee.ecnu.edu.cn)

<sup>b)</sup>Electronic mail: [zghu@ee.ecnu.edu.cn](mailto:zghu@ee.ecnu.edu.cn)

## ABSTRACT

High-quality and large-area 1T-VSe<sub>2</sub> nanosheets with different thicknesses on flat mica substrates are grown by ambient-pressure chemical vapor deposition. Temperature-dependent Raman spectra between 90 and 350 K have been performed to investigate the phenomena of the charge density wave (CDW) order. It can be found that the frequency of the A<sub>1g</sub> mode increases with the decreasing temperature. When the temperature reaches 110 K, the A<sub>1g</sub> mode abruptly converts to a low wavenumber. This phenomenon proves the CDW formation of VSe<sub>2</sub> with the 5 nm thickness. It can be interpreted as arising from an enhanced electron-phonon coupling mechanism. Moreover, variable temperature-dependent Raman spectra for VSe<sub>2</sub> with different thicknesses showed that the phase transition temperature gradually increased with the thickness. In addition, the CDW phase transition has also been detected by the abrupt change of the resistance, and its slope is located at about 112 K. The present results can be helpful for the potential applications of VSe<sub>2</sub> crystals, such as spintronics devices and supercapacitors.

Published under license by AIP Publishing. <https://doi.org/10.1063/1.5135038>

A typical conductive two-dimensional (2D) material is metallic transition metal dichalcogenides (MTMDs).<sup>1,2</sup> MTMDs have emerged due to their intriguing properties, such as superconductivity, ferromagnetism, charge density wave (CDW) order, and so on.<sup>3–6</sup> Among them, vanadium diselenide (VSe<sub>2</sub>) has been widely studied as a typical MTMD material. The strong electron coupling for all adjacent V<sup>4+</sup>-V<sup>4+</sup> pairs in VSe<sub>2</sub> induces its metallic character and the presence of the CDW phase.<sup>7,8</sup> Additionally, an original monolayer VSe<sub>2</sub> exhibits strong room-temperature ferromagnetism and behaves as a unique 2D magnetic material.<sup>9–11</sup> The CDW order for MTMDs becomes a very interesting topic because it refers to the periodic fluctuation of the charge density appearing in the crystal. Although many hypotheses are proposed to explain it, the origin and tuning of the CDW order still remain a mystery.<sup>12–14</sup> According to the previous work, the strong interaction between the electron and the phonon is considered to be the most convincing explanation for the CDW

order.<sup>15–17</sup> As we know, the ambient-pressure chemical vapor deposition (APCVD) technique has been extended to the synthesis of MTMDs.<sup>18</sup> Nevertheless, the explorations of large-area and thickness-adjustable fabrication of MTMDs are still in progress.

In the Letter, we are committed to exploring the preparation of VSe<sub>2</sub> nanoflakes and investigating the optical and electrical properties. We design an APCVD route for the direct synthesis of the high-quality and large-area 1T-VSe<sub>2</sub> films to gain an insight into the CDW order. Moreover, the CDW phase transition of the synthesized VSe<sub>2</sub> nanosheets has been confirmed by the combination of Raman spectra and electrical measurement.

The fluorophlogopite mica and VSe<sub>2</sub> have the same triple lattice symmetry. Thus, mica can be used as the substrate to support the epitaxial growth of VSe<sub>2</sub> nanosheets.<sup>19,20</sup> As shown in Fig. 1(a), we use a two-zone chemical vapor deposition (CVD) furnace with separate temperature controls to grow the VSe<sub>2</sub> nanosheets. Commercial VCl<sub>3</sub>

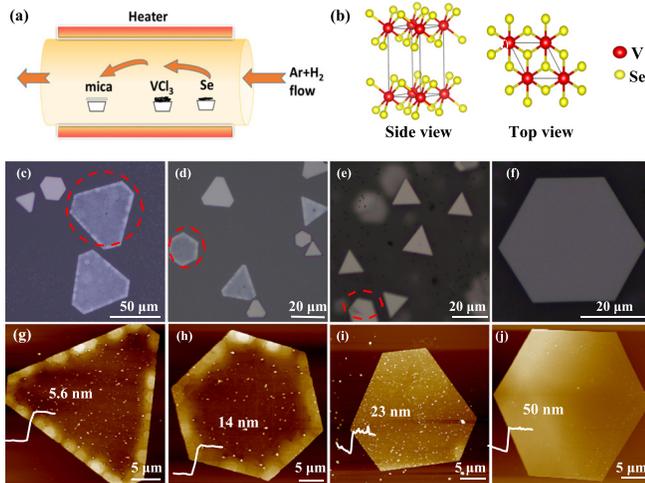


**FIG. 1.** (a) Illustrations of the synthesis setup. (b) The crystal structure of 1T-VSe<sub>2</sub>. (c)–(f) OM images of 1T-VSe<sub>2</sub>. (g)–(j) AFM images of 1T-VSe<sub>2</sub>. Note that the samples marked by the red dashed lines in (c)–(f) are selected to check the thicknesses by AFM. On the other hand, the white solid lines at the flake borders in (g)–(j) suggest the thickness curves of the samples.

powders were placed in the middle of the first zone of the furnace at the upstream end (source zone). The Se powders were placed on the edge of the source zone. The mica substrates with freshly cleaved surfaces were placed in the downstream area (substrate zone, 10 cm from VCl<sub>3</sub>). After loading all the precursors, the tube was sealed and purged with a mixed 200 sccm Ar/H<sub>2</sub> flow for 20 min. Then, the source zone and the substrate zone were heated up to 550 and 650 °C, respectively. These temperatures were held at their respective setpoints of 10 min. After the deposition, the furnace was cooled to room temperature naturally. The crystal structure of VSe<sub>2</sub> is plotted in Fig. 1(b).

The morphologies of 1T-VSe<sub>2</sub> crystals are shown in Figs. 1(c)–1(j). Optical microscopy (OM) and atomic force microscopy (AFM) measurements were performed to evaluate the morphology, size, and thickness evolution of 1T-VSe<sub>2</sub>. These samples were grown at different Ar/H<sub>2</sub> flow rates, which are varied from 50 sccm to 200 sccm. From the OM images in Figs. 1(c)–1(e), it can be clearly seen that VSe<sub>2</sub> triangles and hexagons were selectively deposited on the mica substrates. No matter how thick the films are, they have both triangular and hexagonal shapes. The distinguished shapes of these polygons are a preliminary sign for the high crystallinity. These samples marked by red dashed lines in Figs. 1(c)–1(e) are selected to test their thicknesses. Obviously, we can see that the size of VSe<sub>2</sub> crystals is about 40 μm. The AFM images are used to identify the thicknesses of the VSe<sub>2</sub> crystals in Figs. 1(g)–1(j). The white solid lines at the flake borders in Figs. 1(g)–1(j) are the thickness curves of the samples. The thicknesses of the VSe<sub>2</sub> nanosheets on mica substrates can be varied from 5.6 to 50 nm.

Figure 2(a) shows the Raman spectra of the hexagonal and triangular VSe<sub>2</sub> nanoflakes grown on the mica. For two-types of VSe<sub>2</sub> nanosheets, a distinct Raman peak can be found at about 203.3 cm<sup>-1</sup>. This peak corresponds to the Raman-active A<sub>1g</sub> mode of 1T-VSe<sub>2</sub>.<sup>8</sup> The weak peak at about 260 cm<sup>-1</sup> originates from the mica substrate. Moreover, the visible photoluminescence signal cannot be detected from the VSe<sub>2</sub> nanoflakes. This phenomenon is consistent with the

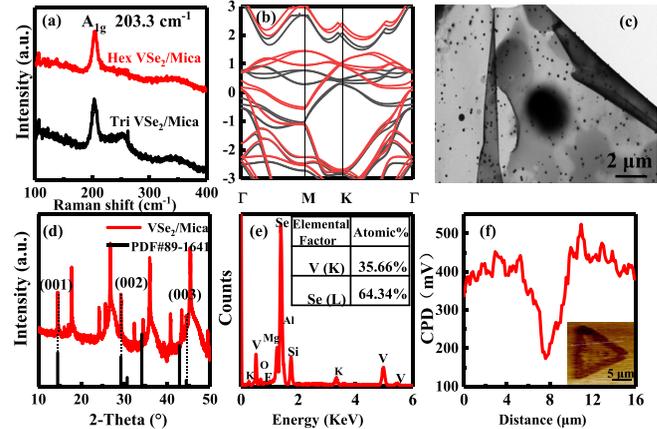


**FIG. 2.** Phase structure identification of VSe<sub>2</sub> polygons. (a) Raman spectra of the as-grown hexagonal (red) and triangular (black) VSe<sub>2</sub> nanosheets on mica. (b) The band structure for a few layer VSe<sub>2</sub>. (c) The TEM image of the ultrathin VSe<sub>2</sub> nanosheet. (d) XRD pattern of VSe<sub>2</sub> nanosheets on the mica substrate. Data from JCPDS card No. 89-1641 are shown at the bottom for comparison. (e) EDS spectrum of VSe<sub>2</sub> and the inset show the proportion of V and Se elements. (f) KPFM image of VSe<sub>2</sub>.

zero-forbidden band characteristic of the 1T-VSe<sub>2</sub>.<sup>21</sup> This is also in good agreement with the band diagram calculated in Fig. 2(b). A band crossing the Fermi energy indicates that 1T-VSe<sub>2</sub> is metallic. To identify the morphology of the synthesized VSe<sub>2</sub> nanosheets, transmission electron microscopy (TEM) was also employed for the transferred samples. The TEM image of typical few layer VSe<sub>2</sub> nanosheets is presented in Fig. 2(c). The high electron transmittance arises from the ultrathin feature of CVD-synthesized VSe<sub>2</sub> nanosheets. The x-ray diffraction (XRD) pattern of the VSe<sub>2</sub> nanosheets is shown in Fig. 2(d). Three main diffraction peaks can be assigned to the (001), (002), and (003) planes of the 1T-VSe<sub>2</sub> crystals according to the Joint Committee on Powder Diffraction Standards (JCPDS) card No. 089-1641.<sup>22,23</sup> The other peaks are from the mica substrate. It indicates that the VSe<sub>2</sub> nanosheets grow along the *c*-axis. This preferential growth is perpendicular to the substrate. In short, the CVD-synthesized triangular and hexagonal VSe<sub>2</sub> nanosheets show the same 1T phase structure and have high crystallinity.

As shown from the energy-dispersive x-ray spectroscopy (EDS) in Fig. 2(e), the peaks from V and Se elements can be observed. The atomic ratio of V to Se is about 1:1.8, which is approximate to the ideal stoichiometric value. It was confirmed that the obtained VSe<sub>2</sub> nanosheets were the products of VCl<sub>3</sub> and Se. The Kelvin Probe Force Microscopy (KPFM) image of VSe<sub>2</sub> is shown in Fig. 2(f). We can see that the surface potential on the edge of the sample is higher than that in the middle. It is consistent with the van der Waals epitaxial growth mode of VSe<sub>2</sub>. That is to say, the metallic VSe<sub>2</sub> nanosheets tend to nucleate at edge regions and extend into the energetically favorable center region.<sup>24</sup>

Figure 3(a) reveals the temperature-dependent Raman spectra of the 5 nm thick triangular VSe<sub>2</sub> film. In order to explain the relationship between the internal structural changes and the domain evolution, the temperature effects were removed from the Raman spectra. Then, they were fitted with Gaussian and Lorentzian peaks in the

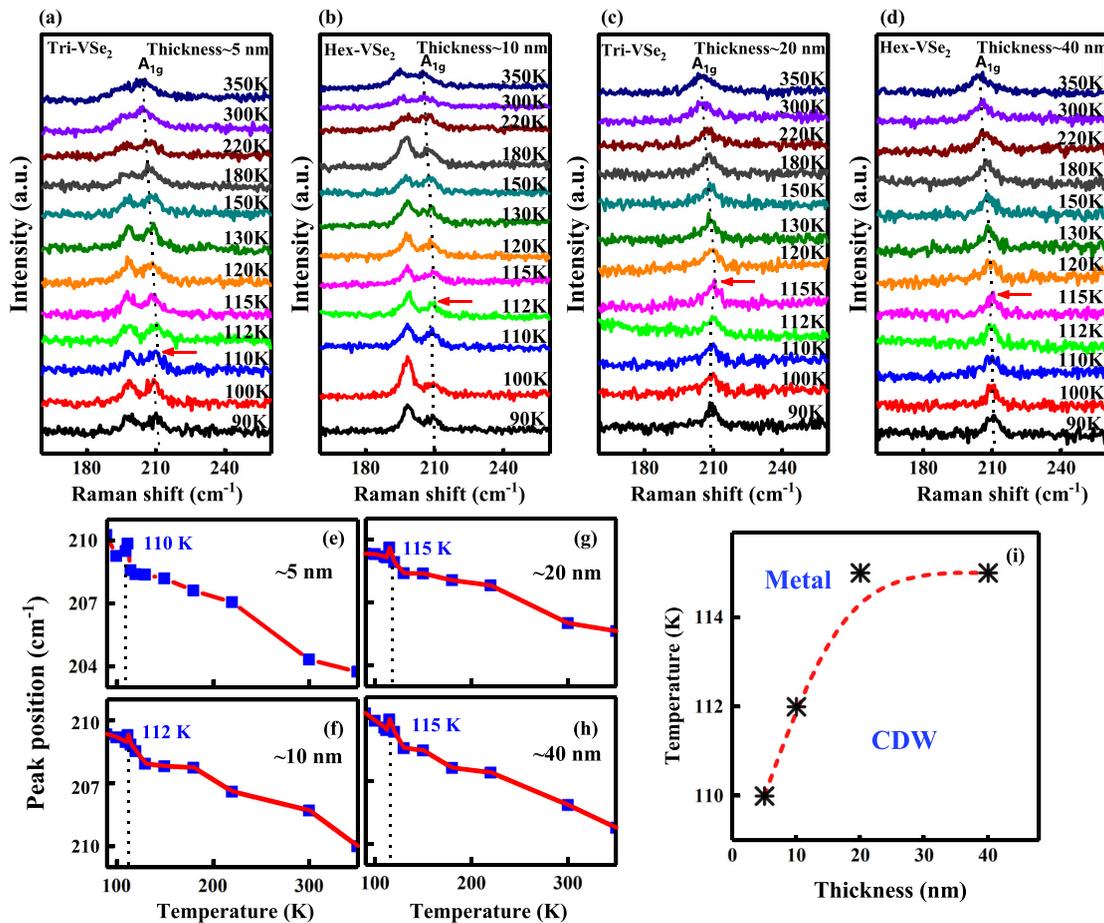


**FIG. 3.** The phase diagram of the CDW transition temperature of 1T-VSe<sub>2</sub> achieved by variable-temperature Raman spectroscopy. Temperature-dependent Raman spectra of (a) 5 nm thick triangular, (b) 10 nm thick hexagonal, (c) 20 nm thick triangular, and (d) 40 nm thick hexagonal VSe<sub>2</sub>. Peak position plots of the A<sub>1g</sub> mode for (e) 5 nm thick triangular, (f) 10 nm thick hexagonal, (g) 20 nm thick triangular, and (h) 40 nm thick hexagonal VSe<sub>2</sub> as a function of temperature. (i) The phase diagram of CDW transition temperature with the layer thickness for 1T-VSe<sub>2</sub>.

frequency range between 160 and 250 cm<sup>-1</sup>. Note that a Raman characteristic peak (A<sub>1g</sub>) appears in both the normal metallic phase and the CDW phase. Interestingly, the A<sub>1g</sub> mode, which corresponds to the out-of-plane vibration of two Se atoms around one V atom initially, shifts to a higher wavenumber during the cooling process. This phenomenon may be due to the hardening of the phonon with the decreasing temperature. The electron-phonon interaction results from an electron scattering off an ion, creating a phonon and an electron absorbing a phonon at an ionic site. The selenium atoms induce vibrations in the phonon modes with the increasing temperature, which is mostly due to the effect of the anharmonicity and the influence of the thermal expansion or the volume contribution. However, upon further cooling at about 110 K, the A<sub>1g</sub> mode shifts to a lower wavenumber. The change may be due to the formation of the CDW super-lattice, which causes a lateral phonon to fold from the L point of the Brillouin zone edge to the center of the zone. As the temperature drops further from 110 K to 90 K, the A<sub>1g</sub> mode shifts to a higher wavenumber. The frequency of the A<sub>1g</sub> mode is plotted as a function of temperature, as shown in Fig. 3(e). The frequency of the A<sub>1g</sub> mode decreases abruptly

when the temperature drops to 110 K. This temperature point is near to the critical temperature of the phase transition from the metallic phase to the CDW phase. The phase transition temperature is consistent with the reported CDW phase transition temperature at about 112 K.<sup>25</sup> In order to further understand the thickness-dependence of the CDW transition temperature, temperature-dependent Raman spectroscopy measurements were also carried out on 1T-VSe<sub>2</sub> nanoflakes with the thicknesses of about 10 nm, 20 nm, and 40 nm, as shown in Figs. 3(b)–3(d), respectively. The frequencies of the observed Raman modes (A<sub>1g</sub>) are also plotted as a function of temperature shown in Figs. 3(f)–3(h), respectively. As the layer thickness decreases from 40 nm to 5 nm, it can be seen that the CDW transition temperature also decreases gradually. It may be due to the excess V atoms in the van der Waals gap between layers. Such defects affect the formation of the CDW.

Although the electrical resistance of VSe<sub>2</sub> as a function of temperature and film thickness has already been studied,<sup>26</sup> the systematic Raman spectroscopy results have not been reported before. Note that the previous studies reported that the CDW phase transition temperature points were all located at about 80 K. However, the CDW phase

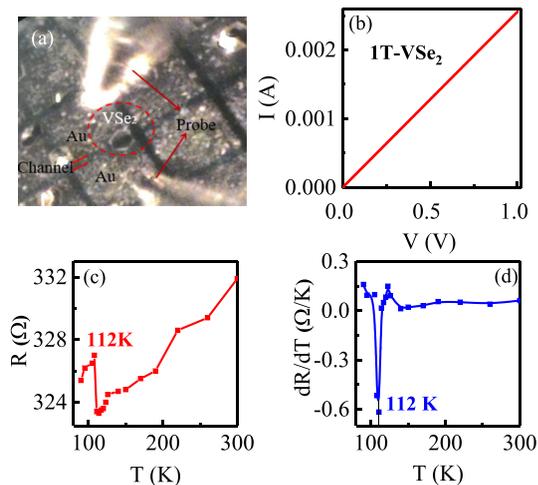


**FIG. 4.** Electrical measurements of 1T-VSe<sub>2</sub>. (a) The experimental setup for the Ohmic contact. (b) The function between the current (*I*) and the voltage (*V*) of VSe<sub>2</sub> at room temperature. (c) The function between the resistance and the temperature of VSe<sub>2</sub>. (d) The function between the differential resistance and the temperature of VSe<sub>2</sub>.

transition temperature can be observed at about 110 K in the present work. According to the previous work, two phase transitions in 1T-VSe<sub>2</sub> have been discovered.<sup>7</sup> A 3q-state formed at 110 K can be transformed into an irregular pattern of 2q-domains at 80 K. Additionally, it may be related to the preparation method of the samples. These VSe<sub>2</sub> films in the present work were prepared by APCVD. However, these materials were obtained by the mechanical exfoliation method in the previous study.

To corroborate the CDW transition temperature, the electrical properties were also executed on 1T-VSe<sub>2</sub> films, as shown in Fig. 4. Figure 4(a) shows the configuration of the 1T-VSe<sub>2</sub> films and Au electrodes, which were patterned onto films by thermal evaporation. The contacts are at the top of the nanosheet. The residual resistance ratio (RRR =  $R_{300K}/R_{90K}$ ) of the sample is about 1.02. For different voltage sweeping, the current–voltage (*I*–*V*) curve represents the Ohmic contact between the electrodes and the materials, as shown in Fig. 4(b). As plotted in Fig. 4(c), the resistance gradually decreases as the temperature decreases, indicating that the electron–phonon scattering is dominant. However, the resistance bends upward at about 112 K. This phenomenon corresponds to the CDW transition. It indicates that the CDW formation results in the modulation of the electronic structure, which heavily impacts the electronic transport properties. The electron–phonon scattering is effectively reduced by the strongly coupled CDW modulation. The function between the differential resistance and temperature of 1T-VSe<sub>2</sub> shown in Fig. 4(d) reveals that the CDW transition temperature is also located at about 112 K. This transition temperature matches well with that measured from Raman spectra.

In conclusion, we have synthesized large-area and tunable-thickness 1T-VSe<sub>2</sub> on the mica substrates through the APCVD method. We have unambiguously visualized the transition from the normal metallic phase to the CDW phase according to the temperature-dependent Raman spectra and electrical measurement. More significantly, the CDW transition temperature will decrease with

the decreasing thickness. Our investigation can provide fundamental spectroscopy and electrical information for 2D 1T-VSe<sub>2</sub> crystals.

This work was financially supported by the National Key R&D Program of China (Grant Nos. 2018YFB0406500, 2019YFB2203403, and 2017YFA0303403), the Natural Science Foundation of China (Grant Nos. 91833303, 61974043, and 61674057), the Projects of Science and Technology Commission of Shanghai Municipality (Grant Nos. 18JC1412400, 18YF1407200, 18YF1407000, and 19511120100), and the Program for Professor of Special Appointment (Eastern Scholar) at Shanghai Institutions of Higher Learning.

## REFERENCES

- J. D. Zhou, J. H. Lin, X. W. Huang, Y. Zhou, Y. Chen, J. Xia, H. Wang, Y. Xie, H. M. Yu, J. C. Lei, D. Wu, F. C. Liu, Q. D. Fu, Q. S. Zeng, C.-H. Hsu, C. L. Yang, L. Lu, T. Yu, Z. X. Shen, H. Lin, B. I. Yakobson, Q. Liu, K. Suenaga, G. T. Liu, and Z. Liu, *Nature* **556**, 355 (2018).
- R. A. Klemm, *Physica C* **514**, 86 (2015).
- G. Duvjir, B. K. Choi, I. Jang, S. Ulstrup, S. Kang, T. T. Ly, S. Kim, Y. H. Choi, C. Jozwiak, A. Bostwick, E. Rotenberg, J. G. Park, R. Sankar, K. S. Kim, J. Kim, and Y. J. Chang, *Nano Lett.* **18**, 5432 (2018).
- X. Y. Chia, A. Ambrosi, P. Lazar, Z. Sofer, and M. Pumera, *J. Mater. Chem.* **4**, 14241 (2016).
- W. W. Zhao, B. H. Dong, Z. L. Guo, G. Su, R. J. Gao, W. Wang, and L. X. Cao, *Chem. Commun.* **52**, 9228 (2016).
- W. Y. Tong, S. J. Gong, X. G. Wan, and C. G. Duan, *Nat. Commun.* **7**, 13612 (2016).
- D. J. Eaglesham, R. L. Withers, and D. M. Bird, *J. Phys. C* **19**, 359 (1986).
- Z. P. Zhang, J. J. Niu, P. F. Yang, Y. Gong, Q. Q. Ji, J. P. Shi, Q. Y. Fang, S. L. Jiang, H. Li, X. B. Zhou, L. Gu, X. S. Wu, and Y. F. Zhang, *Adv. Mater.* **29**, 1702359 (2017).
- K. Xu, P. Chen, X. Li, C. Wu, Y. Guo, J. Zhao, X. Wu, and Y. Xie, *Angew. Chem., Int. Ed.* **52**, 10477 (2013).
- M. Bonilla, S. Kolekar, Y. J. Ma, H. C. Diaz, V. Kalappattil, R. Das, T. Eggers, H. R. Gutierrez, M. H. Phan, and M. Batzill, *Nat. Nanotechnol.* **13**, 289 (2018).
- Y. D. Ma, Y. Dai, M. Guo, C. W. Niu, Y. T. Zhu, and B. B. Huang, *ACS Nano* **6**, 1695 (2012).
- T. M. Rice and G. K. Scott, *Phys. Rev. Lett.* **35**, 120 (1975).
- T. Straub, T. Finteis, R. Claessen, P. Steiner, S. Hufner, P. Blaha, C. S. Oglesby, and E. Bucher, *Phys. Rev. Lett.* **82**, 4504 (1999).
- M. N. Faraggi, X. Zubizarreta, A. Arnau, and V. M. Silkin, *J. Phys.: Condens. Matter* **28**, 184004 (2016).
- T. Valla, A. V. Fedorov, P. D. Johnson, P. A. Glans, C. McGuinness, K. E. Smith, E. Y. Andrei, and H. Berger, *Phys. Rev. Lett.* **92**, 086401 (2004).
- K. Zhang, Z. Y. Cao, and X. J. Chen, *Appl. Phys. Lett.* **114**, 141901 (2019).
- R. T. Lv, J. A. Robinson, R. E. Schaak, D. Sun, Y. F. Sun, T. E. Mallouk, and M. Terrones, *Acc. Chem. Res.* **48**, 56 (2015).
- A. L. Hector, M. Jura, W. Levason, S. D. Reid, and G. Reid, *New J. Chem.* **33**, 641 (2009).
- H. Li, J. Cao, W. Zheng, Y. Chen, D. Wu, W. Dang, K. Wang, H. Peng, and Z. Liu, *J. Am. Chem. Soc.* **134**, 6132 (2012).
- J. Ji, X. Song, J. Liu, Z. Yan, C. Huo, S. Zhang, M. Su, L. Liao, W. Wang, Z. Ni, Y. Hao, and H. Zeng, *Nat. Commun.* **7**, 13352 (2016).
- F. Li, K. Tu, and Z. Chen, *J. Phys. Chem. C* **118**, 21264 (2014).
- M. Chhowalla, H. S. Shin, G. Eda, L.-J. Li, K. P. Loh, and H. Zhang, *Nat. Chem.* **5**, 263 (2013).
- H. Zhang, L. M. Liu, and W. M. Lau, *J. Mater. Chem. A* **1**, 10821 (2013).
- Z. P. Zhang, Y. Gong, X. L. Zou, P. R. Liu, P. F. Yang, J. P. Shi, L. Y. Zhao, Q. Zhang, L. Gu, and Y. F. Zhang, *ACS Nano* **13**, 885 (2019).
- N. D. Boscher, C. S. Blackman, C. J. Carmalt, I. P. Parkin, and A. G. Prieto, *Appl. Surf. Sci.* **253**, 6041 (2007).
- J. Y. Yang, W. K. Wang, Y. Liu, H. F. Du, W. Ning, G. L. Zheng, C. M. Jin, Y. Y. Han, N. Wang, Z. R. Yang, M. L. Tian, and Y. H. Zhang, *Appl. Phys. Lett.* **105**, 063109 (2014).